Spring 2023

Using Mineral Magnetism to Characterize Compositions of Fe-Ti Oxide Phases of the Sulphur Creek Lava Flow (Kulshan)

Elika Zilis

Using Mineral Magnetism to Characterize Compositions of Fe-Ti Oxide Phases of the Sulphur Creek Lava Flow (Kulshan)

Elika Zilis

Advised by Dr. Bernie Housen
Collaboration with Dr. Cristina Garcia-Lasanta and Dr. Michael Kraft
June 2023
Geology Department, Western Washington University, 516 High St., Bellingham, Washington, 98225
Scientific Technical Services, Western Washington University, 516 High St., Bellingham, Washington, 98225
Honors College, Western Washington University, 516 High St., Bellingham, Washington, 98225

Abstract

The aim of this study is to examine variations in the composition of Fe-Ti oxide minerals in the Sulphur Creek lava flow (SE margin of Kulshan), using magnetic techniques and electron microscopy. Geochemical and petrological data from these rocks dated ~9.8 ka may be a product of two distinct magma pulses (Garvey, 2022) with two distinct compositions: andesitic basalt and basalt. The composition of cubic oxides (magnetite and ulvöspinel) is influenced by the geochemistry of the crystallizing magma and can be used to provide information about the chemical evolution of these magmas, but also to help frame future paleomagnetic studies of these flows that can determine the temporal history of their emplacement. In this study, I asses the utility of electron microscopy for identifying precise chemical compositions on the micro-scale and the comparison of the results to those of magnetic experiments. The amount of titanium (Ti) in the magnetite (Fe_3O_4) - ulvöspinel (Fe_2TiO_4) solid solution series is directly manifested in its Curie temperature; the temperature at which the grains lose their ability to be permanently magnetized. The Curie temperature of samples from the Sulphur Creek flows were determined using thermomagnetic experiments, which were then used to estimate the composition of these titanomagnetites. These were then compared with the Fe and Ti content of phases observed using the electron microscope equipped with an energy-dispersive (EDS) detector. This study produced different results for some of the samples within the andesitic basalt composition between the two methods described above. Reasons for the discrepancy can be inferred by the domain state of the grains, their magnetic behavior, and the limitations of the energy-dispersive detector on the SEM for the smallest sized grains of Fe-Ti oxides. In addition, I provide data for how the rock magnetic properties are different throughout the flow as an aid in future analyses.

Keywords & Definitions:

Kulshan (Mount Baker): Kulshan is a part of the Cascade Volcanic Arc and the northernmost volcano in Washington. Koma Kulshan or Kulshan is the name given to the volcano by indigenous peoples of the Lummi and Skagit tribes where Kulshan means "white sentinel" and the Nooksack tribe where Kulshan means "white mountain" (Beckey, 1995). I refer to the volcano as Kulshan as I respectfully acknowledge Western Washington University's campus is on stolen lands and I am committed to promoting equity in the future.

Magnetic susceptibility, Magnetite, Ulvöspinel

Introduction:

The Sulphur Creek Lava flow is the most recent effusive eruption of Kulshan ~10,000 years ago. Due to its recent age, studying this eruption can give insight to Kulshan's venting processes to help us better prepare for future activity. There are two distinct compositions within this flow that are well identified: andesitic basalt closer to the volcanic source and basalt at the toe of the flow (Garvey, 2022 and references therein). The goal of my study is to investigate how these different compositions are reflected in the iron-titanium oxide minerals as well as asses the validity of comparing data acquired through electron microscopy and that of magnetic experiments to draw parallelisms about these compositional differences. More detailed analysis on these compositions yields insight on the timing and possible cooling conditions of the flow, if it seems to resemble a more distinct boundary between compositions or a gradual change throughout the flow.

Magnetic techniques are an effective method to measure the properties of rocks, sediments, meteorites, and soils in a timely manner and help to identify magnetic mineralogy, grain size, and shape of the ferromagnetic minerals (e.g., Muxworthy et al., 2023). Titanomagnetite- Cubic Fe-Ti oxide minerals that occur along the magnetite-ulvöspinel solid-solution line are the most common carriers of magnetization in mafic volcanic rocks. Ilmenite and hematite form a similar solid-solution series, both consisting of rhombohedral Fe-Ti-oxides. Titanium atoms substitute for iron atoms within magnetite and hematite crystal lattices which are important ferromagnetic minerals due to their high concentration of iron. The more titanium within the magnetite (Fe_3O_4), the closer the titanomagnetite phase is to the opposite end member of the magnetite-ulvöspinel solid solution series (being ulvöspinel Fe_2TiO_4). Temperature vs. magnetic susceptibility experiments help identify different Curie temperatures of the titanomagnetite phase and can be used to estimate chemical compositions of these minerals. The more titanium in the sample, the lower the Curie temperature, as seen by a negative correlation between Curie temperature and the amount of ulvöspinel (e.g., Lattard et al., 2006). These results can then be used to reconstruct the crystallization and alteration history of the basaltic rock (Zhou et al., 2000).

Compositions of these minerals can also be estimated using the JEOL scanning electron microscope (SEM) and AZtec software at WWU and will be used to compare with the magnetic vs. susceptibility measurements for the respective compositions.

Geologic Setting:

Kulshan (Mount Baker) is an Andesitic stratovolcano situated 25 km south of the Canadian border and 50 km east of Bellingham (Hildreth et al., 2003; Figure 1). It is the tallest peak within the North Cascades mountain range with an elevation of 3,285 meters (10,781 feet). Kulshan is thought to be the most eruptive center within the Garibaldi volcanic belt, a Quaternary multivent volcanic field that has been active since ~1.3 Ma (Hildreth et al., 2003). It is a high threat volcano as it is close to large population centers and has abundant glacial ice cover; yet the eruptive products are understudied (Garvey, 2022).

Due to the eastward subduction of the Juan De Fuca plate underneath the North American plate, the volcanically active Cascade arc is present in the northwestern United States and part of Canada to the north (Figure 1). Kulshan is situated above a 45 km thick crust (Garvey, 2022 and references therein), while the oceanic slab of the subduction zone is at a depth of ~100-120 km beneath the volcano (Bostock and VanDecar, 1995). The basement primarily consists of Mesozoic and Paleozoic rocks. Rhyodacite and andesite make up 50% of the total eruptive product, while basalt and dacite make up only between 1-3% of the total eruptive product (Hildreth et al., 2003; Figure 2).

The Sulfur Creek lava flow is the youngest effusive eruption of Kulshan (Garvey 2022 and references therein); and has been dated using radiocarbon methods of an underlying tephra to be ~9,800 ka (Scott et al., 2001). It is believed to be the product of a monogenetic effusive eruption (Hildreth et al., 2003) on the southwestern flank of the volcano (Tucker and Scott, 2009), at the Schreiber's Meadow cinder cone and traveled ~12 km down valley towards Baker Lake with a measured volume of 0.5 km^3 (Figure 3).

Methods

Field Work & Sample Collection

Fieldwork was developed during September 2022, and consisted of visiting Mount Baker-Snoqualmie National Forest near Baker Lake to collect small, oriented hand samples from five different sites (Figure 3). Sites 22QSC1 to -3 are deemed to be part of the andesitic section of the flow while 22QSC4 and -5 are part of the basalt section. I also analyzed previously collected data from 19QSC4-6 that are also part of the andesitic section of the flow (Figure 3; Appendix).

JEOL Scanning Electron Microscopy

A total of six thin sections, one per site, were analyzed using the JEOL Scanning Electron Microscope at SciTech Services (WWU). The thin sections have dimensions 12 mm by 25 mm (Figure 4). Three out of six thin sections were assembled by Brendan Garvey for his MS thesis on the same outcrops (see Garvey, 2022). All thin sections were carbon coated before being placed within the SEM.

The JEOL SEM uses energy dispersive x-ray spectroscopy to estimate chemical compositions. The SEM generates an electron beam with a large current and small probe size set to an accelerating voltage to produce high resolution images of individual materials, and the spectroscopic tool can be used to determine chemical composition. The electrons interact with the material (in this case minerals) and generate a photon (x-ray) which has a characteristic level of energy that is proportional to the atomic mass of the material. The energy dispersive spectrometer then detects the energy spectrum of these x-rays (Figure 5). In simpler terms, on a given area on my thin section containing a grain about ~1-3 micron^2 in size, the SEM gives a reading of the elements present and their respective percentages. AZtec is the software that uses a set of factory standards that allows for the EDS quantification.

I surveyed each thin section by doing ~10 “images” on each one corresponding to an area less than 1mm^2. On each image, depending on how many grains that could be titanomagnetite, on average, spectra from nearly 30 grains from each portion of the thin section was studied. This corresponds to about 300 spectra on each thin section. If the area of the grain, however, is too small, the spectra is not accurate, and I discarded these elemental compositions as it did not give the composition that I wanted should it have been titanomagnetite (Figure 6).

I used two methods to determine the fraction of titanium within the oxides analyzed on the SEM to ensure that the values mostly agreed, and my methods were properly done. One method allowed also for the quantification of the Fe^{2+} and Fe^{3+} cation contributions using WinMIgob software (Yavuz, 2021). I used the output from WinMigob to calculate the ulvöspinel÷magnetite ratio. Both methods started with using Aztec software to calculate the oxide weight percentages of the elements present within the grains I analyzed using the EDS detector on the JEOL SEM. The EDS data used by AZtec allows for the quantification of FeO which consists only of Fe^{2+} (not Fe^{3+}) and is calibrated to a set of factory standards for EDS quantification. After I quantified the oxide weight percentages normalized to 100, I put the data from my spectra into excel tables respective to each thin section from a particular site. Each column within the row of a spectrum shows the different element oxide compositions (Appendix).

For the first method, I used Microsoft Excel to calculate the ratio of titanium-oxide out of the total Fe-O + Ti-O content within the sample. I then discarded data that had a total Fe-O + Ti-O percentage that was less than 90% as this is indicative of the spectrum not being a pure enough iron oxide to be useful in

my analysis. I then took the average of the titanium-oxide value of the respective grain to calculate one value of this parameter for each site.

The second method uses the data processing software called WinMIgob, which uses a combination of different charge-balance methods to calculate the respective values of Ti, Fe^{2+}, and Fe^{3+} (Yavuz, 2021). I first input the same excel file from Aztec that I use for the above method using WinMIgob's format which does not include all the elements that were analyzed (Appendix). The combination of methods and calculations I input to the software for my analysis were developed by Stormer, (1983), Anderson and Lindsley (1985), Bacon and Hirschmann (1988) and Ghiorso and Evans (2008). The resulting values of Ti, Fe^{2+}, and Fe^{3+} add to three or very close to three as this is how many cation vacancies are within magnetite (Fe_3O_4) and ulvöspinel (Fe_2TiO_4) as seen from their formulae. I discarded rows of spectra that added to less than 2.65 because, again, this is indicative of a spectrum that is not a pure enough iron-oxide to be useful in my analysis. I then discarded the rows of spectra that had negative Fe^{3+}. This is not possible, and I am inferring these incorrect values are a result of the titanium read on the SEM given by a different mineral such as ilmenite rather than a titanomagnetite, as per Yavuz, (2021). From these data, I calculated Ti/ Ti+Fe^{2+}+Fe^{3+} to obtain the amount of Ti-O for each spectrum and took an average yielding the amount of titanium-oxide from each thin section.

To calculate the average ratio of ulvöspinel present within each thin section from the SEM, I used the values generated from WinMIgob software for each row of spectra into this formula: $X_{ulvöspinel} = 3\,Ti/(Ti + Fe)$, and then calculated the average for each site (Appendix). I used this method for the ratio of ulvöspinel because this formula uses the correct proportions of Ti and Fe atoms in the magnetite-ulvöspinel solid solution substitution (Zhou et al., 2000). In most cases, the Ti + Fe added to less than three which is why it is not just 3(Ti) (Table 4).

Rock Magnetism Experiments

The experiments I have conducted at the Pacific Northwest Paleomagnetism Laboratory at WWU consist of measuring the magnetic susceptibility of the minerals within my samples at varying temperatures and quantifying the magnetic coercivity, magnetic saturation, and remanence of the ferromagnetic minerals present in these same samples.

Magnetic susceptibility vs. Temperature curves

I performed 13 magnetic susceptibility vs. temperature (k-T) curves on the Kappabridge magnetic susceptometer coupled with a furnace using powdered samples ranging between 488 mg and 509 mg from all sites in the study. The magnetic susceptibility of the sample is measured at different temperatures. Magnetic properties of minerals are directly related to temperature, and ferromagnetic minerals have a characteristic temperature called the Curie temperature (T_c), which defines the transition from ferromagnetic to paramagnetic behavior.

During the experiment, the sample is heated from room temperature (~ 22°C) to 700°C, then cooled back to room temperature while a small intensity induced magnetic field is applied to it and a reading of the sample's magnetic susceptibility is measured every ~1.5°C. These experiments were conducted under an argon atmosphere to minimize the occurrence of chemical reactions such as oxidations that can compromise the sample's original magnetic properties by changing its composition upon heating.

The Curie temperatures of the ferromagnetic minerals present in the samples were determined using the intersecting tangents method of Grommé et al. (1969). I drew one line tangent to where the samples begin to lose magnetic susceptibility and another line tangent to the part of the graph that indicates the lowest magnetic susceptibility for the specific mineral phase showing that behavior. The Curie temperature is determined by the temperature value where the lines intersect (Figure 7).

To calculate the ratio of ulvöspinel from the given Curie temperatures, I used the regression curve $T_c = 150\ X^2_{Usp} - 580\ X_{Usp} + 851$ developed by Bleil et al. (1982) as well as the plot of this curve developed by Lattard et al. (2006) to calculate the average ratio of ulvöspinel present within each site using the lowest Curie temperature present (Figure 13). I analyze the ratio of ulvöspinel for the most Ti-rich phase of titanomagnetite within the sample because the phases that are less Ti-rich have a very small ratio of ulvöspinel (~0.05).

Hysteresis loops

Hysteresis loops were performed on a total 14 samples using the Vibrating Sample Magnetometer (VSM). I prepared powdered samples ranging between 184 mg and 239 mg and placed each in a small gel capsule. The sample is set to vibrate while subjected to a directed magnetic field of variable intensity up to a maximum of 1.0 Tesla (T). First, incremental steps of 5 mT are applied to the maximum 1 T, next a sequence in decreasing intensity is applied on the same direction, and the process is repeated in the opposite direction, to create a hysteresis loop. Measurements of the magnetic moment produced by the sample subjected to those fields are taken after a 200 ms averaging time for each field intensity and are recorded by the VSM Micromag software. On the graph obtained, we can determine the value of the magnetic coercivity (H_c), saturation magnetization (M_s) and the magnetic remanence (M_{rs}). These properties are specific to different populations of ferromagnetic minerals and yield information about their composition and the grain sizes.

Isothermal Remanent Magnetization (IRM) acquisition curves

The same powdered samples from the hysteresis experiments were used to perform IRM acquisition curves, which measure the remanent magnetization acquired by the samples immediately after a field of varied increasing intensity was applied to them. This is an aid to help assess the remnant magnetization (M_r) and coercivity of the remanence (H_{cr}) which we can use in conjunction with the hysteresis results to create a Day plot using the ratios between parameters from the different experiments (Day, 1977).

Results:

Hysteresis & IRM acquisition Curves

I compare the average values of coercivity, magnetic saturation, and remanence by site to understand if these properties change gradually throughout the direction of the flow within the different lithologies (Tables 1 & 2).

Samples from both lithologies demonstrate low coercivity values throughout all samples between 0.001 and 18.1 mT. The values obtained for coercivity follow a very clear pattern of increasing coercivity towards the toe of the flow. Site 22QSC1 has the smallest value of 0.001 mT while Site 22QSC5 has the largest value of 18.1 mT (Table 1).

Site 22QSC1, which is the closest to the source of the flow (Schreiber's Meadow) and is andesitic basalt in composition, has the highest value of magnetic saturation of 7.46E-05 Am^2/kg and 22QSC4 has the lowest value of 2.79E-04 Am^2/kg. The values for this parameter are similar throughout the entire flow (Table 1).

The average values obtained for magnetic remanence are a bit more scattered. 22QSC4 has the highest value of 5.46E-05 Am^2/kg and 22QSC1 Am^2/kg has the lowest value of 2.41E-05. However, 22QSC5 has an intermediate value of 4.03E-05 Am^2/kg among the range from all sites (Table 1). Thus, there is not a visible correlation between increasing values of magnetic remanence with respect to its location within the flow.

Low coercivity ferromagnetic behavior and some paramagnetic behavior are observed by the general shape of the hysteresis loops (Figure 9). Magnetite and titanomagnetite are low coercivity, 'soft', magnetic minerals which are the main ferromagnetic contributors within my samples. IRM acquisition results corroborated the low coercivity of the ferromagnetic minerals present as samples reached saturation under relatively low field intensity (Figure 8). A remanent magnetization kept throughout time is characteristic of ferromagnetic behavior as seen by all corrected hysteresis loops (Figure 9A). The total remanence is only from the ferromagnetic contributors. Paramagnetic and superparamagnetic behavior is observed by some grains being undersaturated as seen by an upslope on the top of the uncorrected hysteresis loop (Figure 9B).

Day Plot

Dunlop (2002) derived and tested equations using the parameters given by the hysteresis and IRM experiments to quantify and predict parameters of the mixture of grain sizes and magnetic domains within rock samples containing magnetite (Figure 10), using the Day Plot (Day et al., 1977). The ratio between the coercivity of remanence and coercivity (H_{cr}/H_c) is plotted on the x-axis while the ratio of the magnetic remanence and saturation from the hysteresis experiments (M_{rs}/M_s) is plotted on the y-axis. These ratios are diagnostic of domain state: superparamagnetic (SP), stable single-domain (SD), pseudo single-domain (PSD), multidomain (MD) or a mixture (Dunlop and Carter-Stiglitz, 2006).

The magnetic hysteresis results indicate that there is a mixture of very fine (10nm) superparamagnetic grains and larger single-domain (~0.1 micron) particles (Figure 10). These results are typical of rapidly-cooled mafic volcanics.

Magnetic susceptibility vs. temperature curves

Temperature vs. magnetic susceptibility measurements are displayed in Figure 11 and Figure 12. The curves from all sites except 22QSC5 (basalt) show at least two Curie temperatures (Figure 11A-F, Figure 12A). Thus, the presence of at least two titanomagnetite phases is interpreted in them. Five out of the nine curves from the andesitic basalt sites point to the presence of three phases (three Curie temperatures distinguished) while the other four curves show two titanomagnetite phases (Table 3). One out of four samples within the basalt sites show two Curie temperatures, while the other three curves have one (Figure 12B-D), which is interpreted as the response of a single titanomagnetite phase present at 22QSC5.

The lowest Curie temperature observed in all studied samples is between a range of 160°C and 310°C. Within this interval, the basalt samples show the lowest values of all the collection (Table 3). Moreover, three of the four basalt samples investigated present exclusively have this lowest Curie temperature. The intermediate Curie temperature observed is between a range of 510°C and 565°C, and it has been detected in sites 22QSC1, 22QSC2, 22QSC3, and 19QSC4 which are all andesitic basalt. The highest Curie temperature is ~580°C indicative of magnetite in 22QSC1, 22QSC2, 22QSC3, 19QSC4, and 22QSC4 (see Table 3).

I represented these results on a plot of $X_{ulvöspinel}$ vs. Curie temperature modified from Lattard et al. (2006; Figure 13). This allows for the quantification of the amount of titanium within my samples provided from this technique, as a ratio of ulvöspinel along the magnetite - ulvöspinel solid solution series in each site. The amount of ulvöspinel deduced from the titanomagnetite phase with the lowest Curie temperature shows increasing ulvöspinel content, and thus titanium from source to toe of the flow (Table 4). This is further demonstrated on a plot of the average lowest Curie temperatures observed from each site vs. distance from the flow source to give insight on how the titanium content changes throughout the flow (Figure 14).

Each drop in magnetic susceptibility is characteristic of different phases of titanomagnetite or magnetite. The dominant Curie temperatures of the most titanium-rich phase of titanomagnetite follow a regular trend of decreasing Curie temperature from the source to the toe of the flow (Figure 14). This indicates that in general, the Fe-oxides of the ulvöspinel - magnetite series in these lithologies are more Ti-rich at larger distances from the source of the flow (the Schreiber's Meadow cinder cone). These results also demonstrate a gradual increase in titanium content with increasing distance rather than a distinct difference in the amount of titanium between the two compositions (andesitic basalt and basalt).

Titanium & ulvöspinel content derived from SEM data

Both methods described earlier were used to calculate the average titanium content per site, but I used only the data from WinMIGob software to calculate the average ulvöspinel content present in each thin section analyzed with the SEM because this software allowed for the separation of the respective cations present.

The average ratio of $\frac{Ti}{Ti+Fe}$ present is 0.22 for the andesitic basalt (closer to the volcanic source) section of the flow and 0.21 for the basalt (further from the volcanic source) section. They are all reasonably close in value and are reported along with their standard deviations in Table 5.

I have plotted histograms of the amount of titanium present within each spectrum for each the two lithologies. According to the SEM results, it is visible that the andesitic basalt (Figure 15) has more grains with a higher ratio of titanium than the basalt (Figure 16). This is a better way to look at this data than the averages as we can see that the basalt portion (farther from the volcanic source) has more grains with a smaller ratio of titanium present according to these SEM results, which is the opposite of what the temperature vs. magnetic susceptibility results showed.

Ulvöspinel ratio is derived from the percentage of titanium using the relationship 3Ti/(Ti+Fe). The values obtained from the two methods do not agree for the andesitic basalt section but have reasonably close values for the basalt section (Table 4).

Discussion & Summary

The results from the hysteresis and IRM acquisition curves confirm the presence of 'soft' ferromagnetic minerals being titanomagnetite and magnetite in all the samples studied. Additionally, the results from the temperature vs. magnetic susceptibility experiments confirm the presence of Ti-enriched phases of magnetite and a phase of magnetite in the studied samples. They also show a gradual increase in titanium within the most Ti-enriched phase (the one that presents the lowest Curie temperatures, and thus contains more ulvöspinel), from the volcanic source to toe (Figure 14). The results from the SEM consistently show a significantly larger ratio of ulvöspinel within the andesitic basalt portion of the flow than this ratio obtained from the Curie temperatures. The basalt sites have values that are more agreeable between the two methods (Table 4). One of the main reasons for this discrepancy can be attributed to the limitations of the energy dispersive (EDS) detector when smallest grain sizes of Ti-Fe oxides are the target. Another reason could be that most of the magnetite present within the andesitic basalt is within the small single domain grains, which did not allow to obtain an accurate spectrum, leading to an underestimation of Fe in that lithology that would lead to an overestimated ulvöspinel content.

The JEOL SEM I used for this project is equipped with an energy-dispersive (EDS) detector to separate the characteristic x-rays of different elements into an energy spectrum. The EDS detector likely did not provide an accurate spectrum for these small grains as elements within the matrix would get picked up on the spectrum rather than only those of the tiny grain. Thus, I could only acquire an accurate energy spectrum from grains that were not of the smallest population present. About 40% of the grains present in my samples are less than 10 nm in diameter. Due to the limitations of the EDS detector when the smallest grain sizes of Ti-Fe oxides are targeted, the SEM analysis in this study did not provide accurate data for these tiny grain size populations present in the andesitic basalt.

Many of these smallest grains are likely single domain ferromagnetic grains. From the hysteresis experiments (Figure 9) and the modified Day plot (Figure 10), I could tell that most of the ferromagnetic signal in the titanomagnetite and magnetite grains within the andesitic basalt section of the flow are single domain. These grains are so small, that they are likely many of the ones that I could not get a signal from at all using the SEM. Had they been picked up, larger values of iron and smaller ratios of $\frac{Ti}{Ti+Fe}$ would have been observed, as magnetite has more iron than titanomagnetite.

The two methods used to calculate the percentage of titanium from the acquired data of the SEM also demonstrate slightly different results. This discrepancy can be attributed to the methods used within the WinMIgob software and some of the titanium belonging to different iron-oxides such as ilmenite

($FeTiO_3$) or rutile (TiO_2). WinMIgob calculates the percentage of Fe^{2+}, Fe^{3+}, and Ti content from the data input. Some values of Fe^{3+} calculated from each thin section were negative which is concerning because this should always be positive or zero, as it represents a percentage of a cation vacancy. These results (see reference for the program) indicate that the analysis likely includes elements from other minerals in the overall result. I discarded these spectra as, according to this, I concluded that they may not be part of the titanomagnetite that I wanted to analyze. Thus, the ratio of TiO/(TiO+FeO) is smaller in all cases using WinMIgob software.

Due to a significant amount of iron not being detected by the SEM analysis within the andesitic basalt section due to its very small grain size, the calculated ulvöspinel content does not agree well with the content interpreted by the Curie temperatures analysis for this section (Table 4). However, the results agree better for the basalt section, which according to the magnetic susceptibility vs temperature data generally contained a single phase of titanomagnetite (Ti-rich, i.e., lowest Curie temperatures; Table 3, Figure 12). Thus, we can infer that the phase of Ti-rich titanomagnetite present in the basalt section consists of larger grains of titanomagnetite which was more accurately detected by the EDS detector while the smaller single domain magnetites within the andesitic basalt section were not.

It is reasonable to draw parallelisms between data acquired through the SEM and data acquired from magnetic experiments when the grains of interest are larger than about 10nm. Otherwise, they yield different results due to the limitations of the energy-dispersive detector.

References:

Andersen D.J., Lindsley D.H. (1985). New (and final!) models for the Ti–magnetite/ilmenite geothermometer and oxygen barometer. Abst AGU 1985 Spring Meeting Eos Transactions. AGU 66 (18), 416.

Banerjee, S. and Burton, B. (1991). *Oxide Minerals: Petrologic and Magnetic Significance*. Mineralogical Society of America edited by Lindsley, D., Chelsea, Michigan.

Beckey, F. (1995). *Cascade Alpine Guide: Climbing and High Routes: Rainy Pass to Fraser River*. Mountaineers Books.

Bleil, U., and Peterson, N. (1982), Magnetic properties of natural minerals, in Numerical Data and Functional Relationships in Science and Technology, Group V: Geophysics and Space Research, edited by Angenheister, G. pp. 308 – 365, Springer, New York.

Bostock, M. G. & VanDecar, J. C. (1995). Upper mantle structure of the northern Cascadia subduction zone. Canadian Journal of Earth Science 32, 1^12.

Dunlop, D. J. (2002). Theory and application of the Day plot (Mrs/Ms versus Hcr/Hc) 1. Theoretical curves and tests using titanomagnetite data. *Journal of Geophysical Research: Solid Earth*, *107*(B3), EPM-4.

Dunlop, D.J., Carter-Stiglitz, B. (2006). "Day Plots of Mixtures of Superparamagnetic, Single-Domain, Pseudosingle-Domain, and Multidomain Magnetites." *Journal of Geophysical Research*.

Garvey, B. (2022). Using Crystal Zoning, Thermobarometry, and MELTS to Elucidate Koma Kulshan's (Mt. Baker) Transcrustal Magma Storage System, Northern Cascade Arc. Western Washington University.

Gromme´, C. S., Wright T. L., and Peck. D.L. (1969), Magnetic properties and oxidation of iron-titanium oxide minerals in Alae and Makaopuhilava lakes, Hawaii,J. Geophys. Res.,74, 5277–5294.

Ghiorso, M.S.(2008) The magnetite–ilmenite database (04GhiorsoDataTable.xls). http://earth.geology.yale. edu/~ajs/SupplementaryData/2008/ (accessed 15.08.20)

Hildreth, W., Fierstein, J., Lanphere, M. (2003). Eruptive history and geochronology of the Mount Baker volcanic field, Washington. *Geological Society of America Bulletin*, *115*(6), 729-764.

Lattard, D., Engelmann, R., Kontny, A., Sauerzapf, U. (2006). Curie temperatures of synthetic titanomagnetites in the Fe-Ti-O system: Effects of composition, crystal chemistry, and thermomagnetic methods. *Journal of Geophysical Research: Solid Earth*, *111*(B12).

Muxworthy et al., (2023). Interpreting High-Temperature Magnetic Susceptibility Data of Natural Systems. *Frontiers in Earth Science*.

Stormer J.C. Jr (1983). The effects of recalculation on estimates of temperature and oxygen fugacity from analyses of multicomponent–iron–titanium oxides. Amer Miner 68: 586–594.

Tabor, R. W., Haugerud, R. A., Hildreth, W., & Brown, E. H. (2003). Geologic map of the Mount Baker 30-by 60-minute quadrangle, Washington. USGS. *SEA*, *500*, 500.

Tucker, D. S., Scott, K. M. (2009). Structures and facies associated with the flow of subaerial basaltic lava into a deep freshwater lake: the Sulphur Creek lava flow, North Cascades, Washington. Journal of Volcanology and Geothermal Research, 185(4), 311-322.

Yavuz, F. (2021). "WinMIgob: A Windows Program for Magneite-Ilmenite Geothermometer and Oxygen Barometer." *Department of Geological Engineering, Istanbul Technical University*.

Zhou, W., Van der Voo, R., Peacor, D.R. and Y. Zhang (2000), Variable Ti content and grain size of titanomagnetite as a function of cooling rate in very young MORB, Earth Planet. Sci. Lett., 179, 9 – 20.

Tables:

Table 1. Average values from hysteresis experiments of magnetic saturation, magnetic remanence, and coercivity arranged by site location closest to farthest from flow source.

Site	Lithology	Saturation (Am^2/kg)	Remanence (Am^2/kg)	Coercivity (Tesla)
22QSC1	Andesitic basalt	7.46E-05	2.41E-05	1.11E-05
22QSC2	Andesitic basalt	1.66E-04	4.71E-05	7.01E-03
22QSC3	Andesitic basalt	1.38E-04	4.05E-05	1.15E-02
19QSC4-6	Andesitic basalt	1.06E-04	3.78E-05	1.20E-02
22QSC4	Basalt	2.24E-04	5.46E-05	1.42E-02
22QSC5	Basalt	1.95E-04	4.03E-05	1.81E-02

Table 2. Average values of magnetic remanence and coercivity from IRM acquisition experiments arranged by site location closest to farthest from the flow source.

Site	Lithology	Remanence (Am^2/kg)	Coercivity (Tesla)
22QSC1	Andesitic basalt	1.76E-05	6.88E-03
22QSC2	Andesitic basalt	4.02E-05	1.53E-02
22QSC3	Andesitic basalt	3.48E-05	1.40E-02
19QSC4-6	Andesitic basalt	3.87E-05	3.47E-02
22QSC4	Basalt	4.76E-05	2.60E-02
22QSC5	Basalt	2.99E-05	9.83E-03

Table 3: Curie temperatures (T_c) from magnetic susceptibility vs. temperature experiments.

Sample	Lithology	Lowest T_c (°C)	Intermediate T_c (°C)	Highest T_c (°C)
22QSC1	Andesitic basalt	270	550	580
22QSC2A	Andesitic basalt	310	565	
22QSC2B	Andesitic basalt	260	560	580
22QSC2D	Andesitic basalt	280	540	580
22QSC3	Andesitic basalt	280	550	580
19QSC4.1	Andesitic basalt	240	515	580
19QSC4.4	Andesitic basalt	260	510	
19QSC5OS	Andesitic basalt	200		580
19QSC6.1B	Andesitic basalt	260		580
22QSC4A	Basalt	220		580
22QSC5A	Basalt	160		
22QSC5B	Basalt	180		
22QSC5C	Basalt	160		

Table 4: Amount of ulvöspinel present within each of the samples determined using the SEM and the Curie temperatures (T_c). The ratio from SEM data is obtained by the formula $X_{ulvöspinel} = {}^{3\,Ti}/_{(Ti+Fe)}$. The ratio from the Curie temperatures is obtained by the regression curve $T_c = 150\ X^2_{Usp} - 580\ X_{Usp} + 851$ (Bleil et al., 1982).

Site/Thin Section	Lithology	$X_{ulvöspinel}$ (SEM)	$X_{ulvöspinel}$ (T_c)
22QSC1	Andesitic basalt	NA	0.47
22QSC2B	Andesitic basalt	0.72	0.45
22QSC2D	Andesitic basalt	0.71	NA
22QSC3	Andesitic basalt	NA	0.46
19QSC4-6	Andesitic basalt	0.60	0.51
22QSC4	Basalt	0.59	0.54
22QSC5	Basalt	0.66	0.60
DT-SC12 (Garvey)	Basalt	0.66	NA

Table 5: Averages and standard deviations reported for the calculations of data from the SEM of the average amount of titanium, Ti/(Ti+Fe), per site using WinMIgob software.

Lithology	Site / Thin Section	Number of observations (n)	Average Ti content (Raw data)	Average Ti Content (WinMIgob)	Standard Deviation (WinMigob)
Andesitic basalt	22QSC2B	105	0.33	0.23	0.02
Andesitic basalt	22QSC2D	97	0.31	0.24	0.02
Andesitic basalt	19QSC4-6	70	0.30	0.20	0.01
Basalt	22QSC4	306	0.22	0.19	0.02
Basalt	22QSC5	39	0.26	0.22	0.04
Basalt	DT-SC12	34	0.23	0.23	0.11

Figures

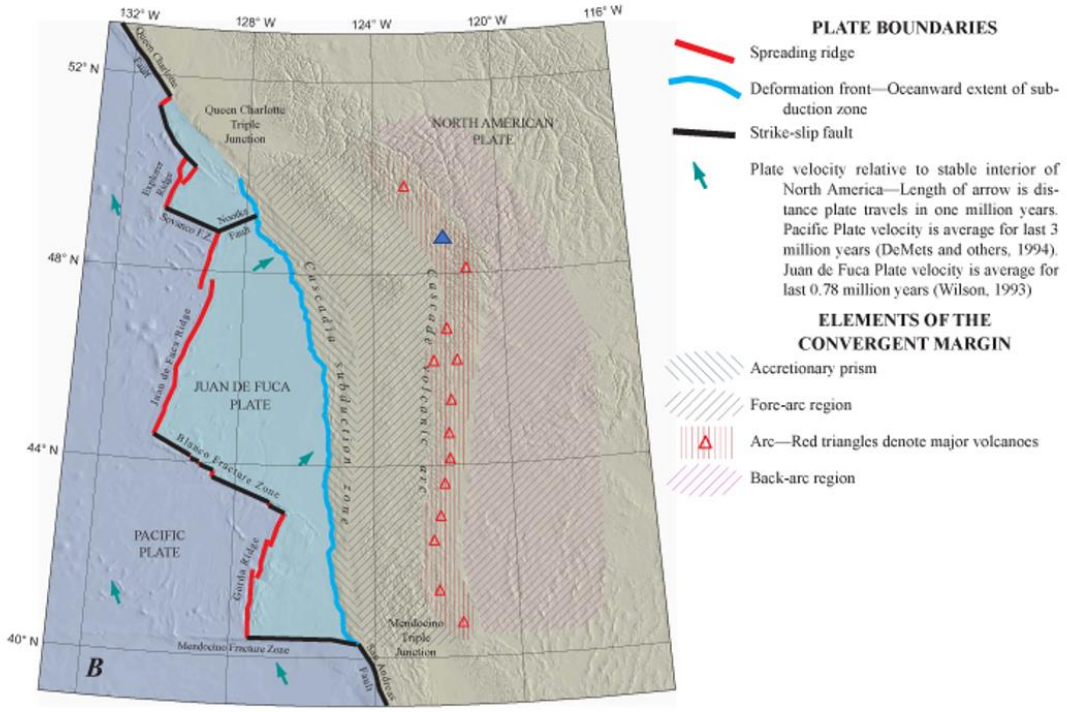

Figure 1: Map of the Cascade Volcanic Arc and Cascadia Subduction Zone with tectonic plates indicated from USGS (Haugerud, 2004).

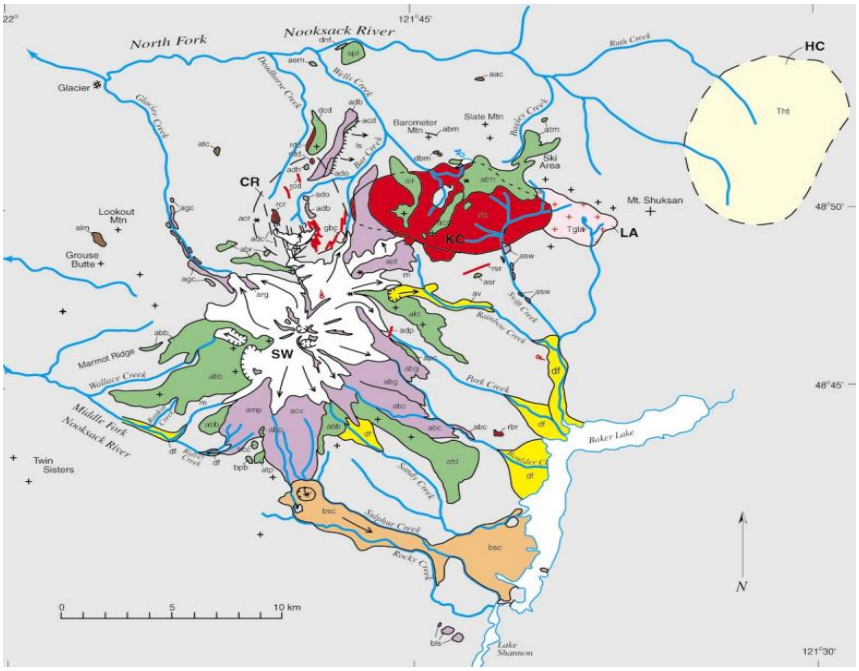

Figure 2: Map of different lava flows from Kulshan throughout its eruptive history. Sulphur Creek is located on the South of the map and represented in orange (taken from Hildreth et al., 2003).

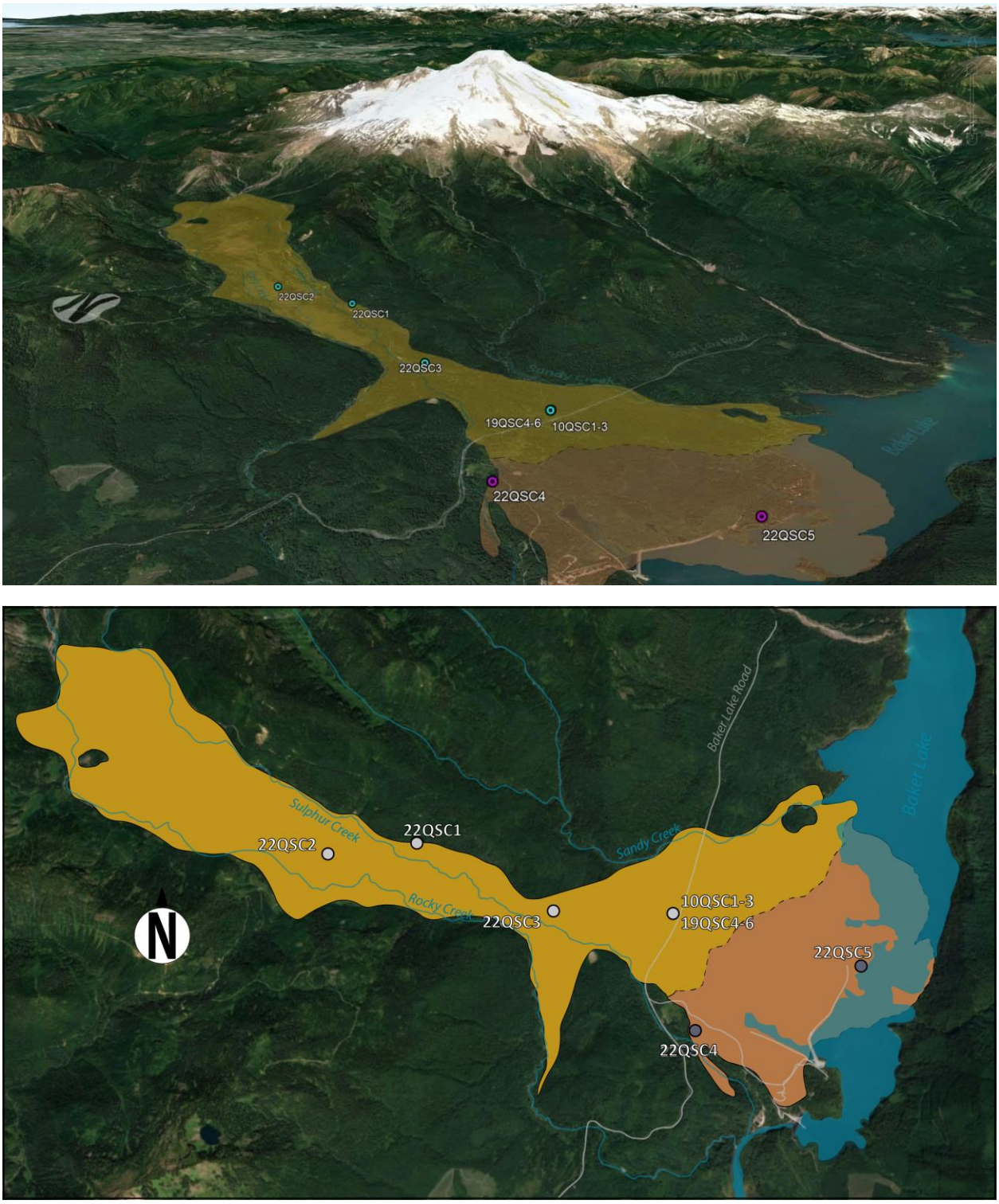

Figure 3: Geologic map showing the Sulphur Creek Lava flow with sites used for this study indicated. Yellow corresponds to the andesitic basalt lithology. Orange corresponds to the basalt lithology (based on Tabor et al., 2003; Tucker and Scott, 2009).

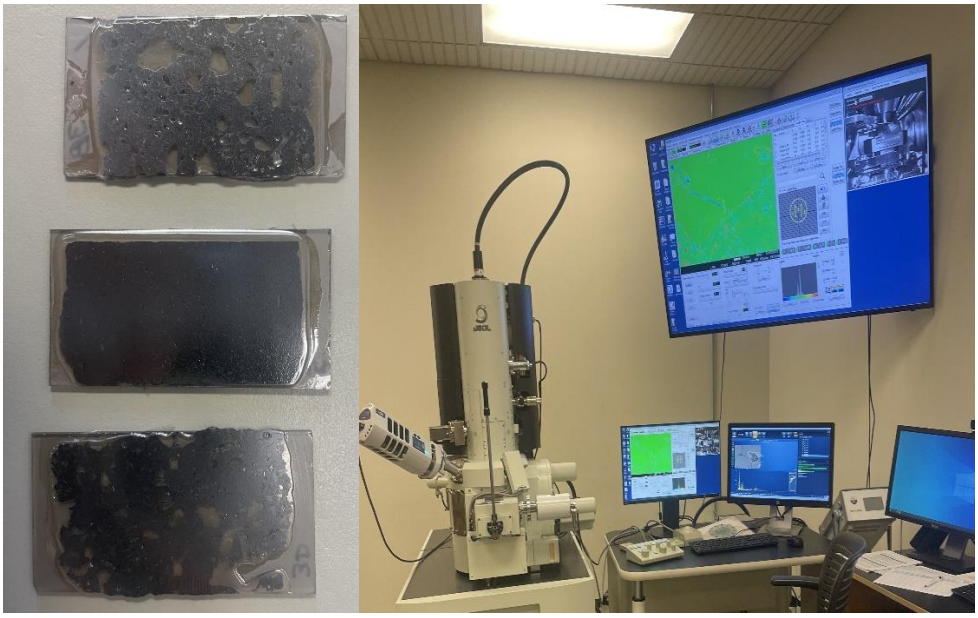

Figure 4: Thin sections I assembled with dimensions 12mm by 25 mm (left). JEOL scanning electron microscope located in CF22 at Western Washington University (right).

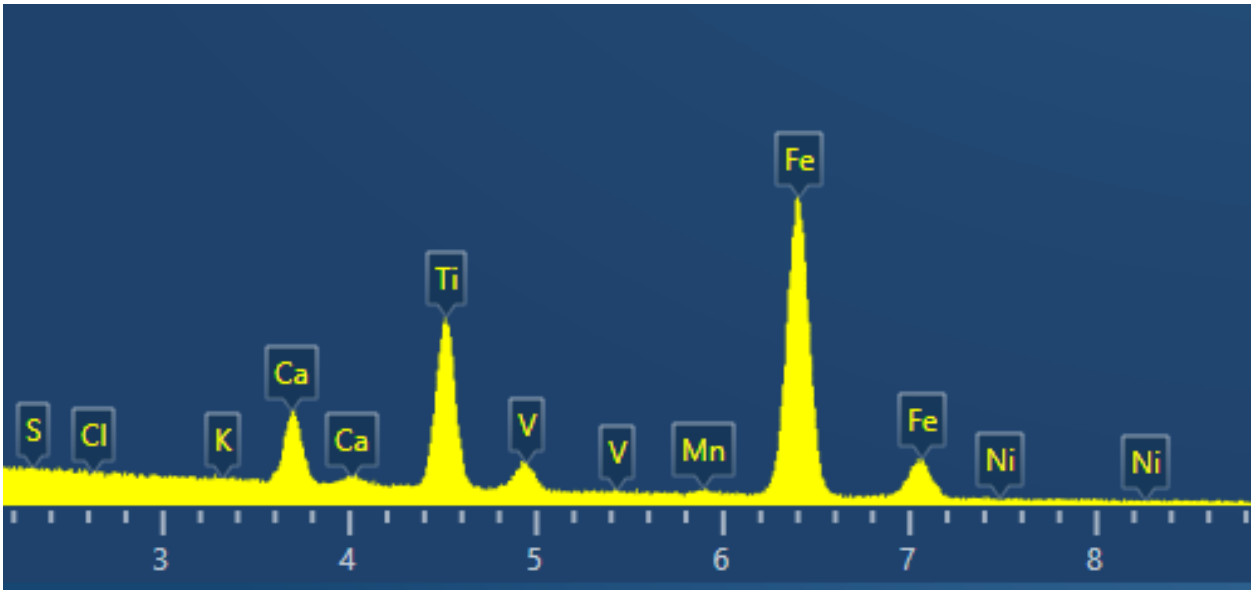

Figure 5: Energy spectrum of x-ray counts vs. energy (keV) displayed by Aztec software using the SEM giving elemental compositions present using the given spectra.

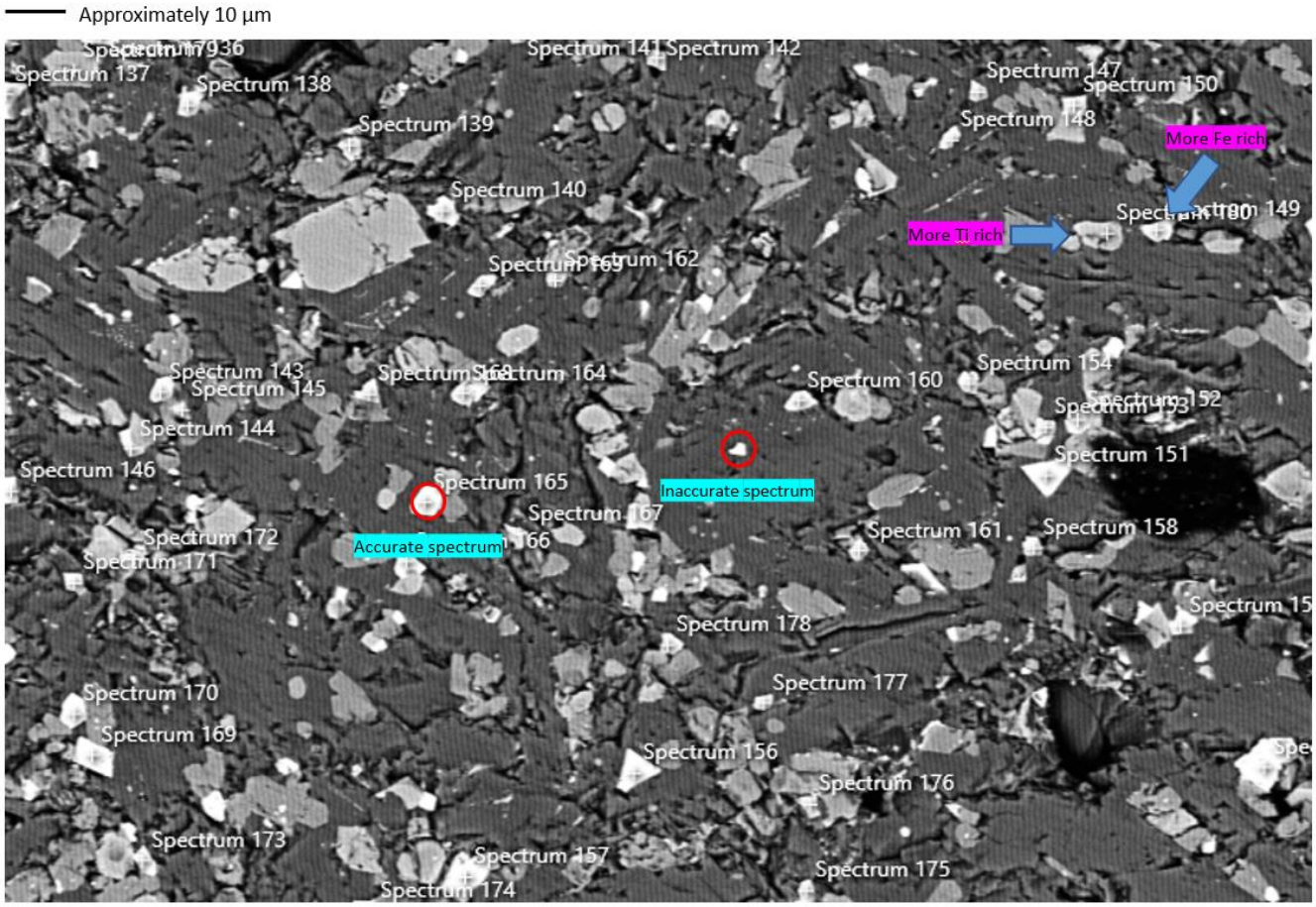

Figure 6A: SEM image showing aquired spectra within an andesitic basat thin section. Grains closer to white are closer to a pure iron oxide while lighter grey grains have more titanium within the iron oxide.

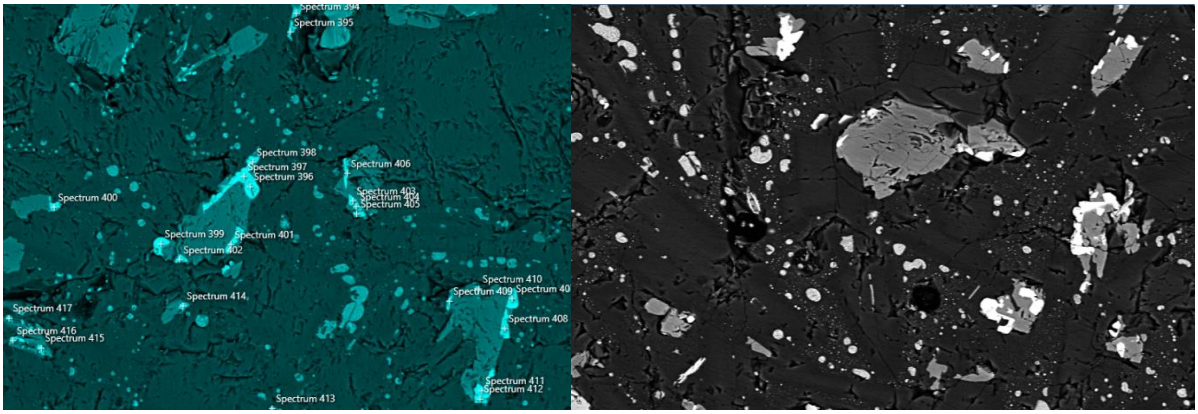

Figure 6B: SEM images of a basalt thin section. The colored filter is used to better detect the grains of interest (left).

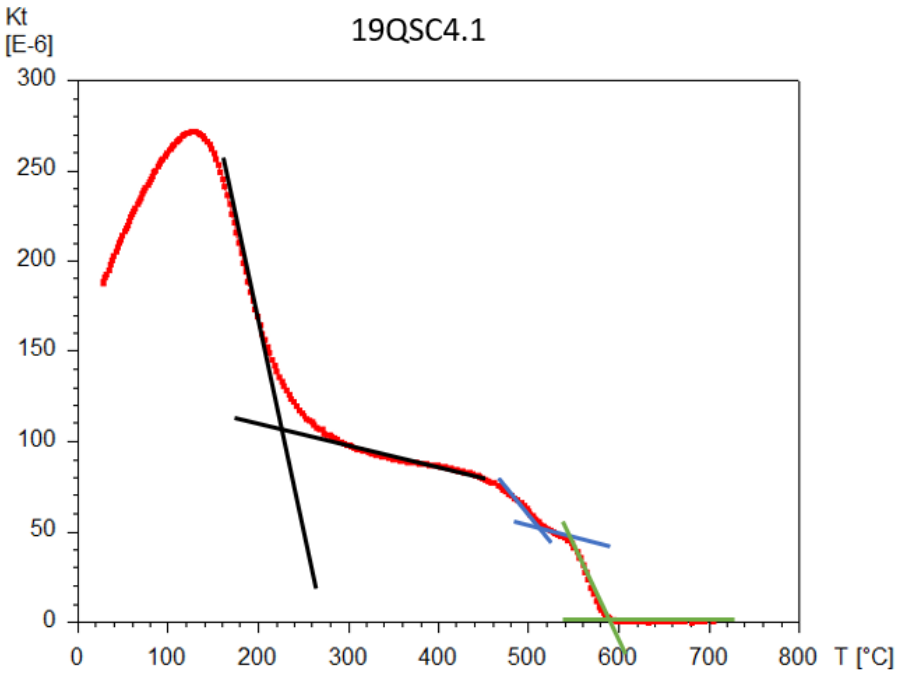

Figure 7: The intersecting tangents method developed by Grommé et al.(1969) to determine the Curie temperatures present within the samples of this study.

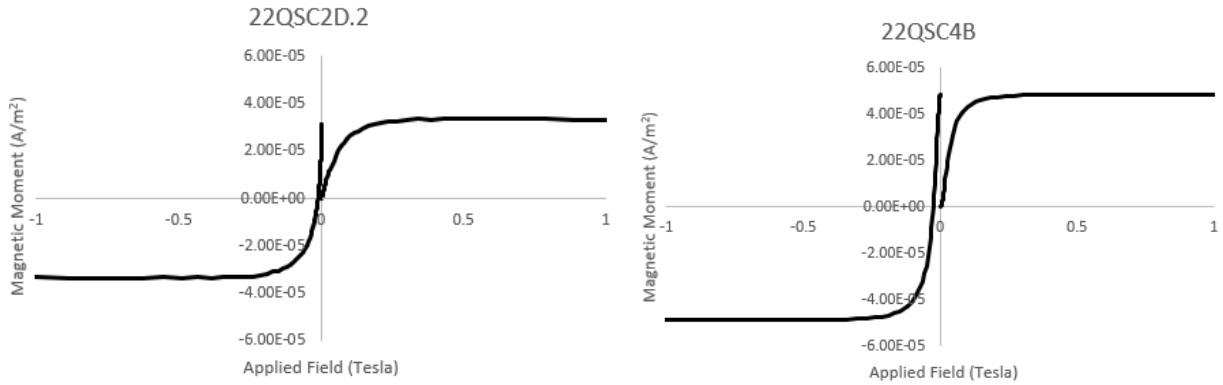

Figure 8: Isothermal remanent (IRM) acquisition curves for andesitic basalt (left) and basalt (right) indicating soft ferromagnetic minerals due to low values of magnetic saturation.

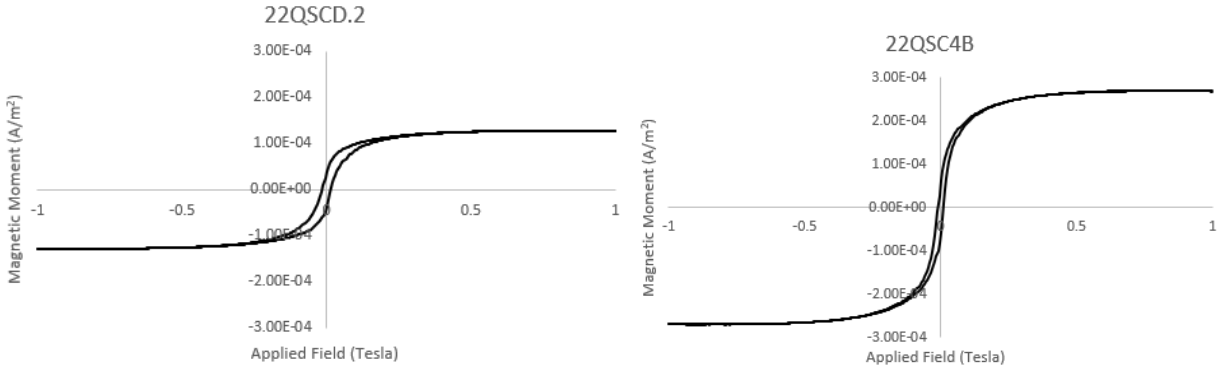

Figure 9A: Corrected hysteresis loops for andesitic basalt (left) and basalt (right).

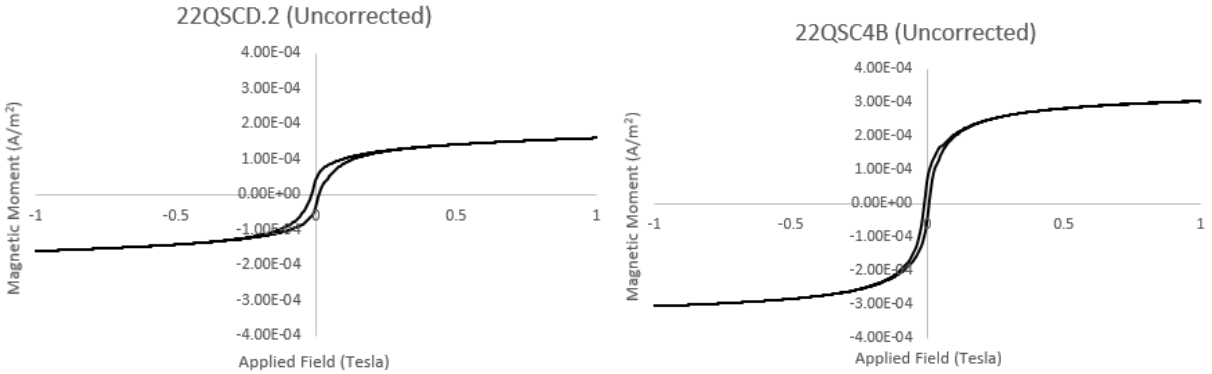

Figure 9B: Hysteresis loops for andesitic basalt (left) and basalt (right) before subtracting the paramagnetic effect to the total magnetic signal.

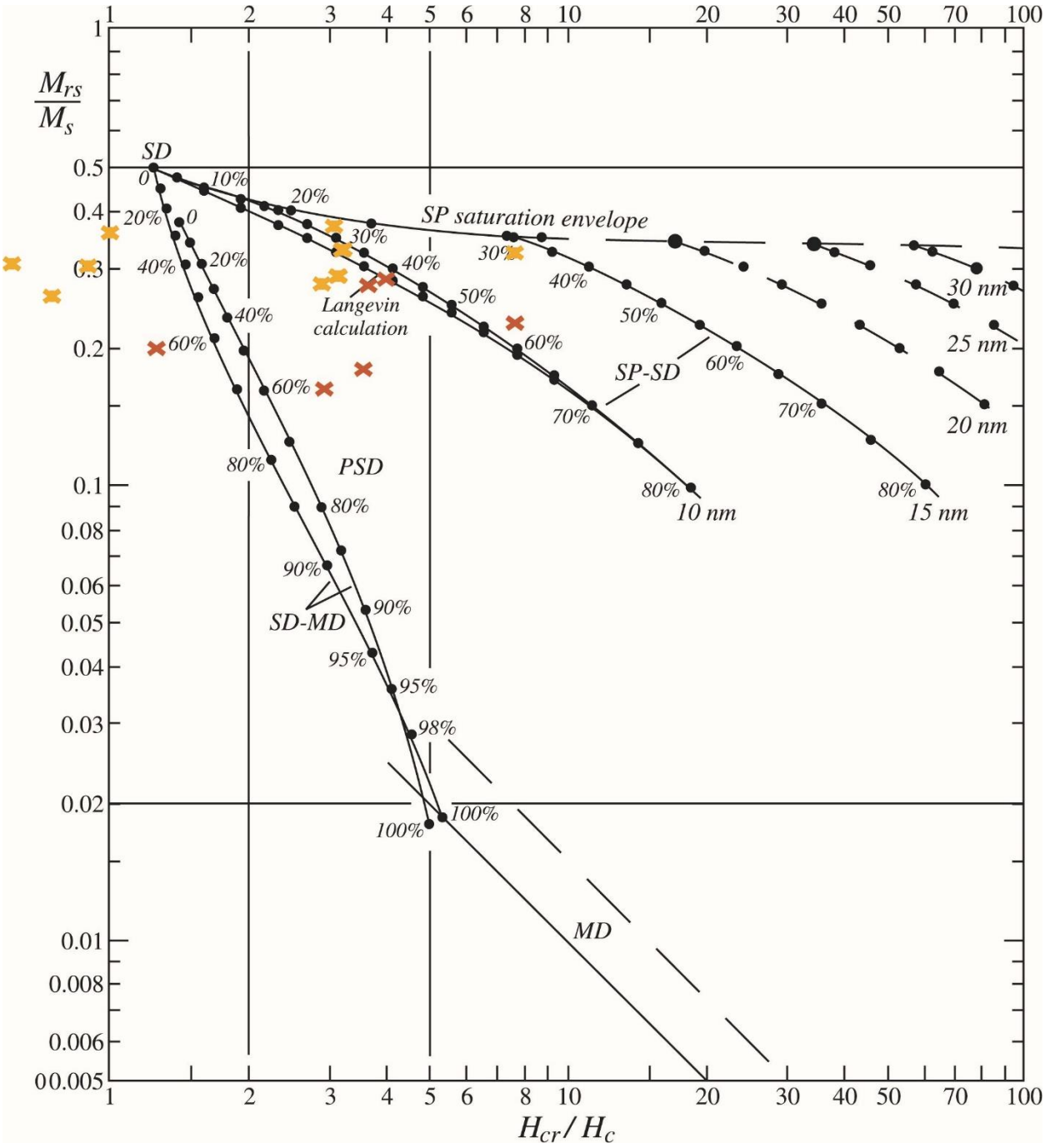

Figure 10. Modified Day plot (Day et al., 1977) from Dunlop, 2002 to characterize magnetic domain state which is proportional to grain size. Yellow dots correspond to samples within the andesitic basalt lithology. Red dots correspond to samples within the basalt lithology.

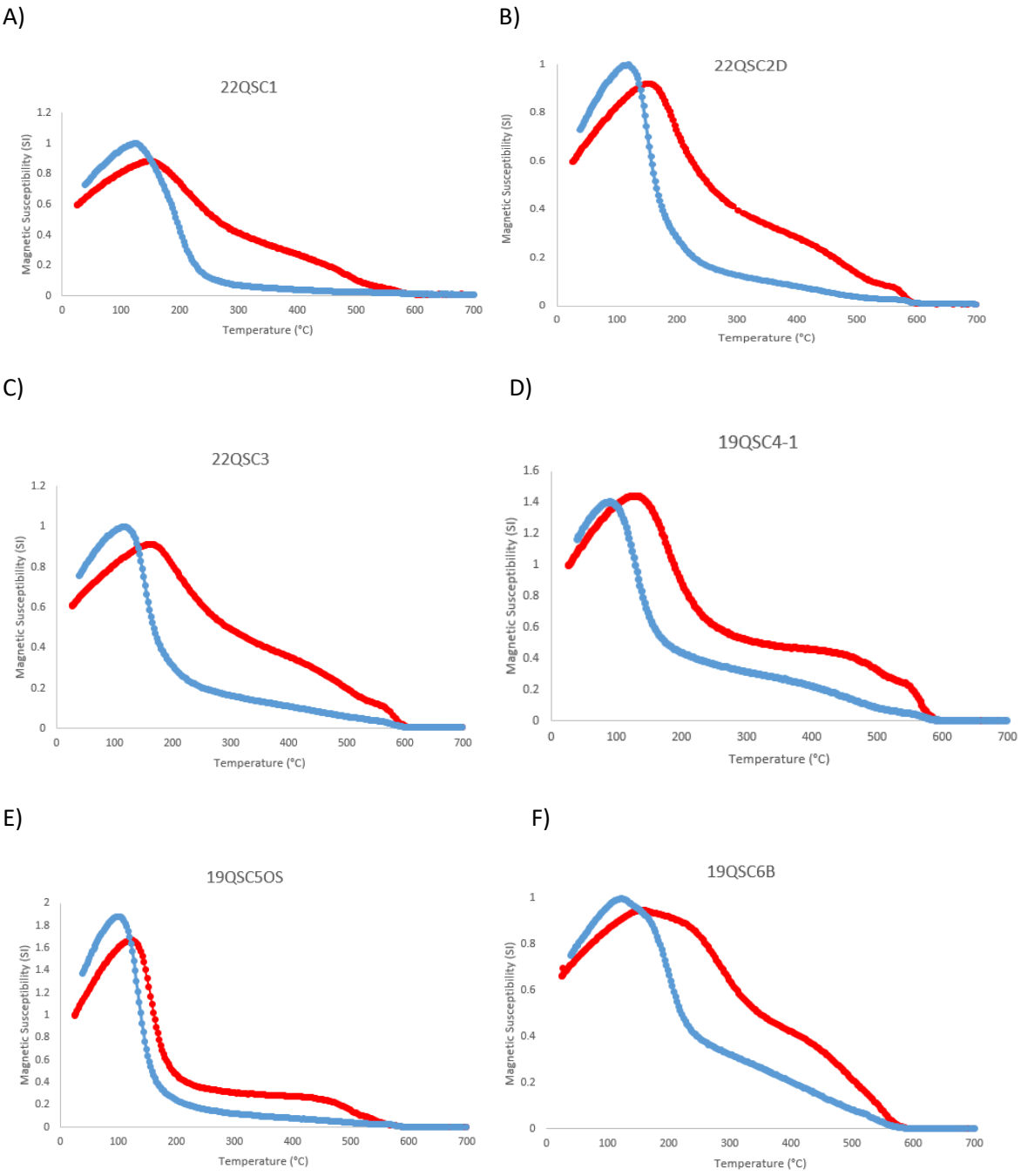

Figure 11: Magnetic susceptibility vs. temperature curves for samples within the andesitic basalt section of the Sulphur Creek lava flow.

A)

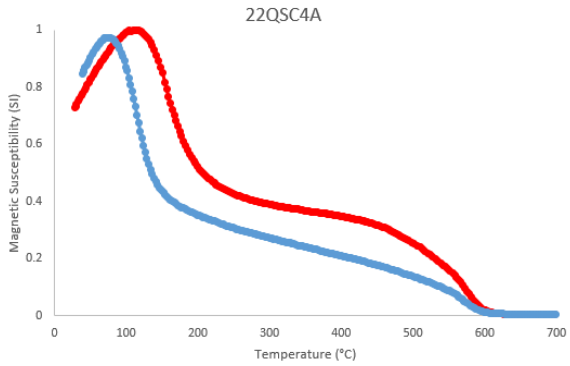

B)

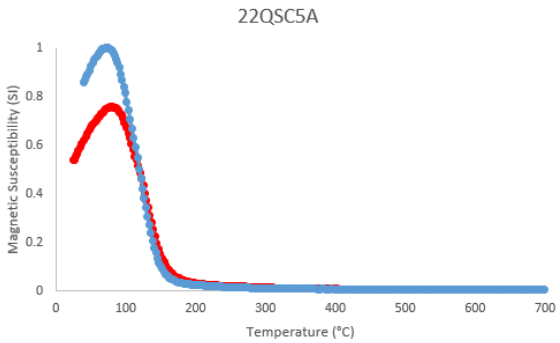

C)

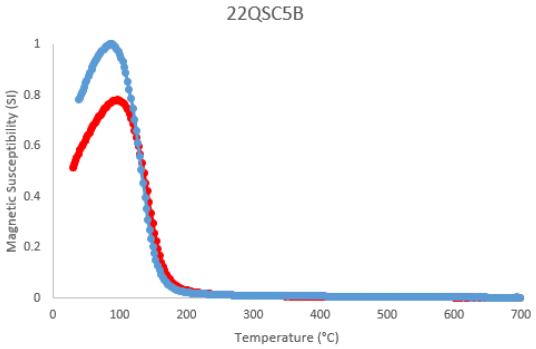

D)

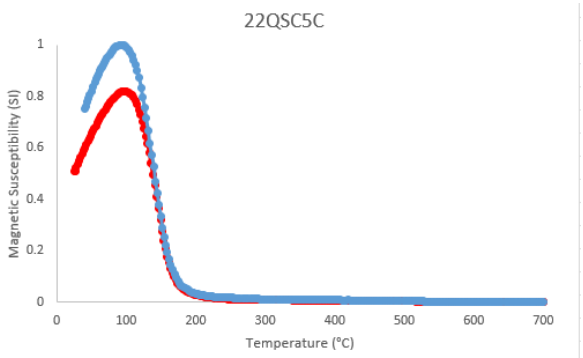

Figure 12: Magnetic susceptibility vs. temperature curves for samples within the basalt section of the Sulphur Creek lava flow.

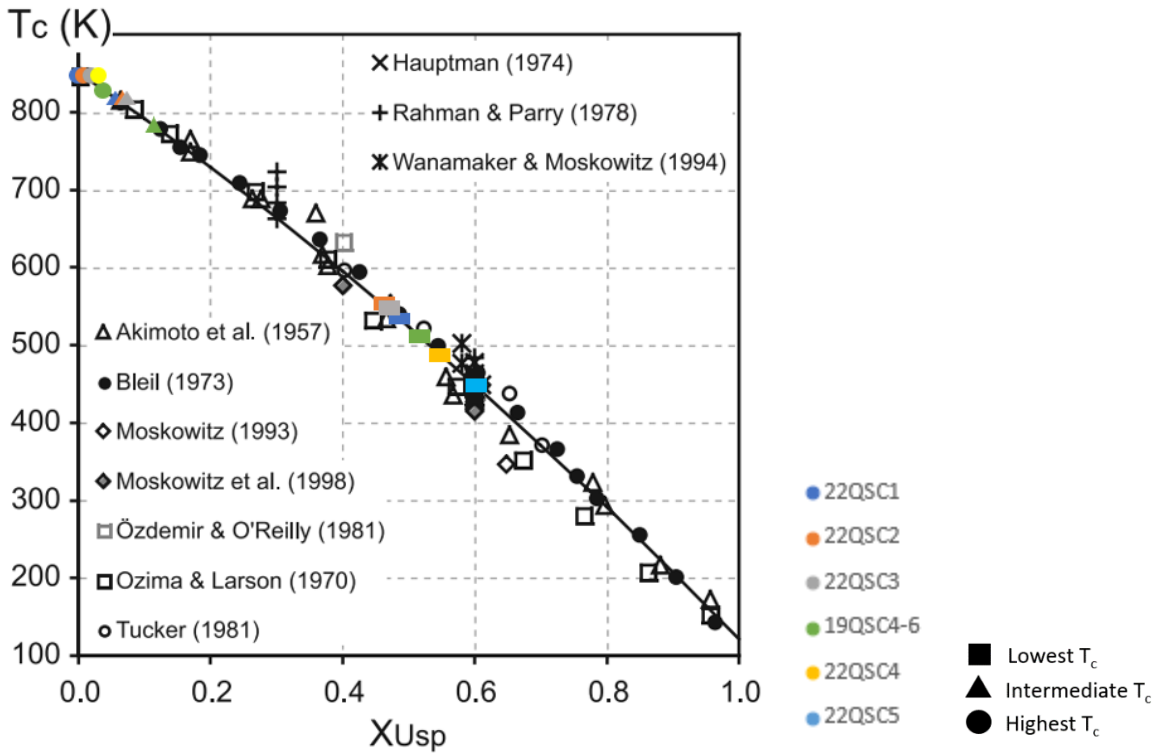

Figure 13: Plot showing Curie temperature from magnetic susceptibility vs. temperature experiments from scientific literature with Curie temperature plotted on the y-axis and ulvöspinel ratio plotted on the x-axis (modified from Lattard et al.,2006). More ulvöspinel corresponds to more titanium within the site. Sites are indicated with different colors shown in legend. The different shapes indicate a different phase of titanomagnetite with different Curie temperatures.

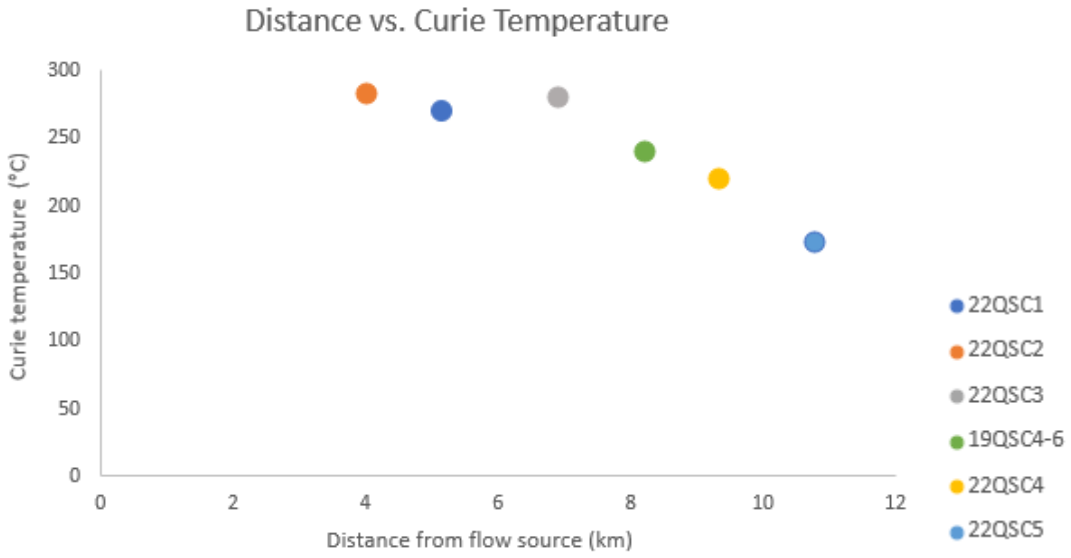

Figure 14: Plot showing the lowest Curie temperature (average per site) present within all samples as a function of distance from the flow source (Schreibers Meadow cinder cone) in kilometers.

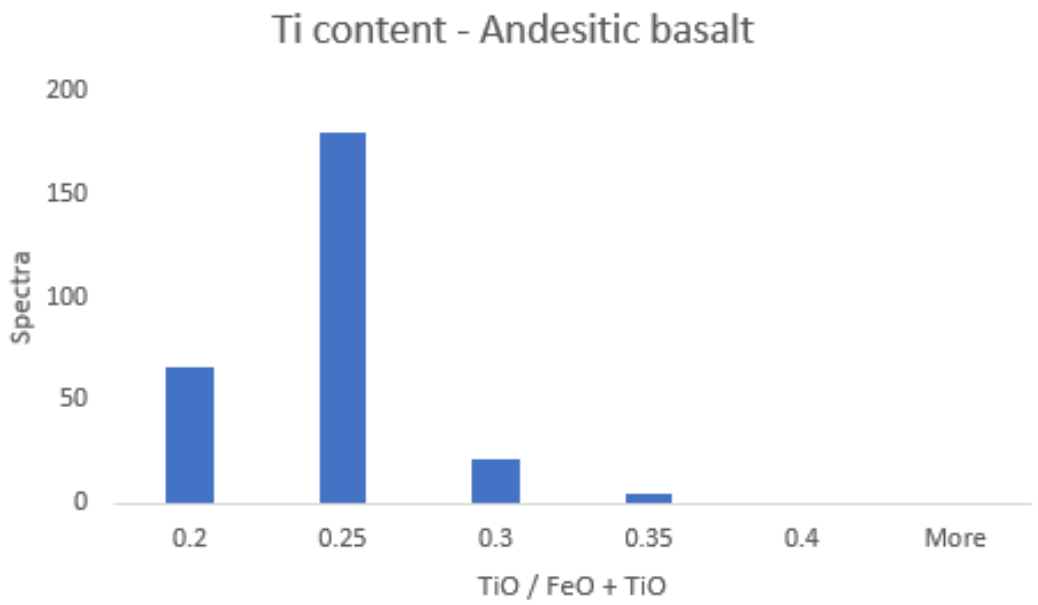

Figure 15: Histogram representing the ratio of titanium present within the andesitic basalt portion of the flow.

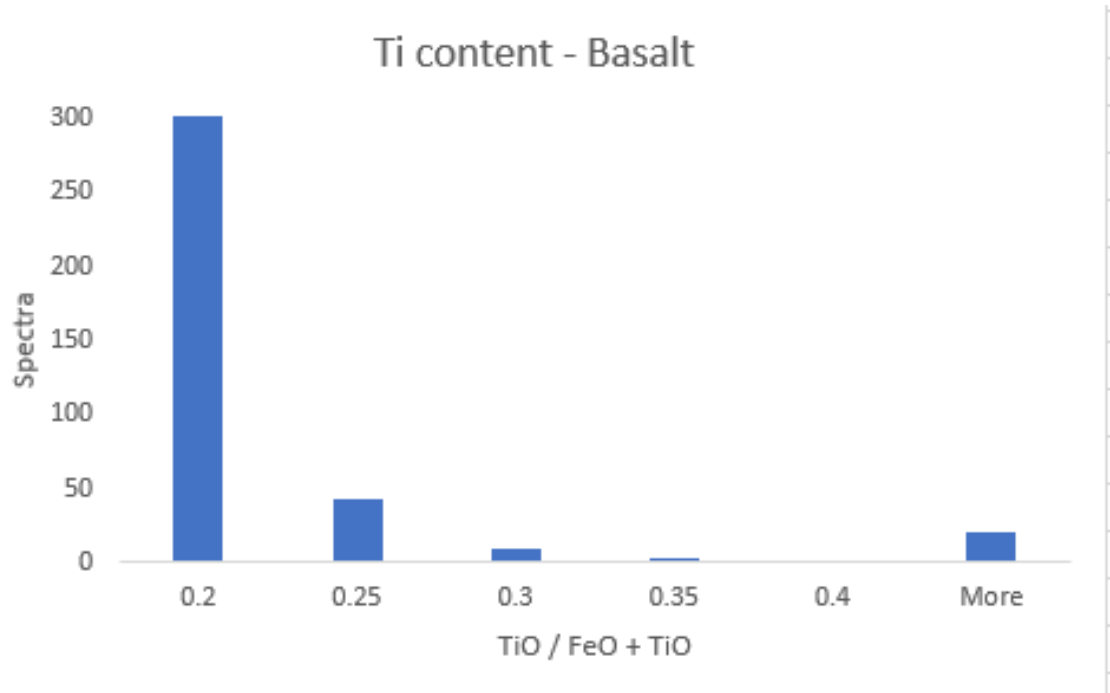

Figure 16: Histogram representing the ratio of titanium present within the basalt portion of the flow.

Appendix:

Samples within the studied sites of my research with given lithology, location, and magnetic experiments performed.

Site	Lithology	Location	k-T Curves	Hysteresis/IRM
10QSC3 19QSC4	Andesitic basalt	48.40°N, 121.42°W	19QSC4-1 19QSC4-4	19QSC4-4
19QSC5	Andesitic basalt	48.40°N, 121.42°W	19QSC5OS	19QSC5-7
19QSC6	Andesitic basalt	48.40°N, 121.42°W	19QSC6-1B	19QSC6.1B
22QSC1	Andesitic basalt	48.68°N, 121.76°W	22QSC1	22QSC1
22QSC2	Andesitic basalt	48.68°N, 121.78°W	22QSC2A 22QSC2B 22QSC2D	22QSC2B 22QSC2B.2 22QSC2D 22QSC2D.2
22QSC3	Andesitic basalt	48.68°N, 121.73°W	22QSC3S	22QSC3 22QSC3B
22QSC4	Basalt	48.66°N, 121.71°W	22QSC4A	22QSC4A 22QSC4B
22QSC5	Basalt	48.67°N, 121.68°W	22QSC5A 22QSC5B 22QSC5C	22QSC5C 22QSC5E

Example data table of elements analyzed for each spectrum using SEM used to calculate TiO ratio without dividing the Ti and Fe into their respective cation contributions (Method #1).

Spectrum Label	Na	Mg	Al	Si	P	S	Cl	K	Ca	Ti	V	Mn	Fe	Ni	Br	Ba	Total	Iron + Ti	TiO/TiO+ FeO
Spectrum 48	0.21	1.33	1.28	1	0.13	0.01	0	0.06	0.26	21.49	0.74	0.56	72.86	0.08			100	94.35	0.2149
Spectrum 49	0.1	1.35	1.24	0.54	0.19	0.06	0	0.08	0.17	21.96	0.76	0.49	73.07	0			100	95.03	0.2196
Spectrum 50	0.18	1.41	1.25	0.65	0.08	0	0	0.08	0.38	21.68	0.86	0.74	72.61	0.08			100	94.29	0.2168
Spectrum 51	0.18	1.83	1.49	0.53	0.1	0.13	0	0	0.46	23.06	0.79	0.63	70.79	0			100	93.85	0.2306
Spectrum 52	0.33	1.61	1.91	2.07	0.15	0	0	0.04	0.57	21.88	0.64	0.57	69.95	0.28			100	91.83	0.2188
Spectrum 53	0.18	1.37	1.44	0.46	0.08	0	0	0.03	0.17	21.36	0.6	0.63	73.63	0.05			100	94.99	0.2136
Spectrum 55	0.16	1.37	1.01	1.4	0.08	0.05	0	0.12	0.29	21.22		0.48	73.75	0			99.95	94.97	0.212306
Spectrum 56	0.47	1.31	2.11	3.32	0	0	0	0.06	0.51	19.46		0.73	71.98	0			99.97	91.44	0.194658
Spectrum 57	0.48	1.31	1.95	7.05	0.03	0	0	0.42	0.52	17.16		0.46	70.52	0.09			99.98	87.68	0.171634
Spectrum 58	0.43	1.53	0.82	2.4	0	0	0	0.11	0.25	44.92	0.99	0.66	46.41	0		1.45	99.99	91.33	0.449245
Spectrum 59	0.16	1.2	1.6	1.85	0.27	0.02	0	0.04	0.83	20.84	0.54	0.66	71.96	0			99.97	92.8	0.208463
Spectrum 62	0.23	1.14	1.51	1.38	0.04	0	0	0.07	0.31	20.28		0.59	74.33	0.12			100	94.61	0.2028
Spectrum 64	0.22	1.56	1.86	0.77	0	0.01	0	0.04	0.34	20.85	0.85	0.42	73.04	0			99.96	93.89	0.208583
Spectrum 65	0.21	1.62	1.68	0.62	0.14	0	0	0.09	0.26	20.67	0.77	0.51	73.42	0			100	94.09	0.2067
Spectrum 73	0.1	1.85	1.37	0.57	0.05	0	0	0	0.19	20.58		0.74	74.38	0.13			99.95	94.96	0.205903
Spectrum 74	0.13	1.92	1.41	0.7	0.13	0.03	0	0.02	0.23	20.65		0.63	74.15	0			100	94.8	0.2065
Spectrum 75	0.17	1.48	1.49	1.01	0	0.04	0	0.15	0.35	18.87	0.85	0.36	75.23	0			100	94.1	0.1887

Example data table of element spectra to input into WinMIgob software.

	A	B	C	D	E	F	G	H	I	J	K	L	M	N	O	P	Q	R	S
1	Row No	Sample No[	SiO2 [M]	TiO2[M]	Al2O3[M]	V2O3[M]	Cr2O3[M]	Nb2O3[M]	Fe2O3[M]	FeO[M]	MnO[M]	NiO[M]	ZnO[M]	MgO[M]	CaO[M]	Na2O[M]	K2O[M]	BaO[M]	
2	1		33.99	0.14	0.17					46.29	0.86	0		18.01	0.31	0.15	0.02		
3	2		35.35	15.84	7.11					35.29	0.24	0		0.77	0.64	2.32	2.24		
4	3		1.53	14.7	1.25					67.2	0.23	0		1.34	7.33	0.23	0.11		
5	4		0.53	47.65	0.25					48.13	0.61	0		2.1	0.25	0.04	0.05		
6	5		2.12	22.15	1.51	0.62				71.11	0.53	0		1.06	0.43	0.35	0.12		
7	6		1.08	19.7	1.2					73.46	0.52	0		1.47	1.17	0.22	0.1		
8	7		0.76	48.09	0.33	0.95				46.54	0.7	0		2.04	0.34	0.14	0.03		
9	8		1.7	46.09	0.53	1.22				45.65	0.61	0		1.8	0.27	0.27	0.15		
10	9		0.79	42.84	0.33	0.85				52.62	0.73	0		1.37	0.19	0.09	0.1		
11	10		3.18	46.34	0.44					45.6	0.73	0		2.47	1.13	0.02	0.04		
12	11		0.74	23.65	1.68	0.93				70.07	0.75	0		1.56	0.24	0.18	0.02		
13	12		2.7	23.51	1.81	1.12				68.08	0.5	0		1.45	0.34	0.24	0.19		
14	13		2.65	67.56	2.18	2.32				20.26	2.24	0		0.88	1.08	0.44	0.08		
15	14		1.8	22.96	1.49					70.07	0.66	0		2	0.51	0.23	0.08		
16	15		0.97	23.7	1.29	0.89				69.99	0.48	0		1.69	0.35	0.23	0.03		
17	16		6.16	21.73	2.51	0.95				65.44	0.51	0		1.35	0.45	0.56	0.32		
18	17		1.78	25.66	2.44	0.78				66.1	0.77	0		1.58	0.39	0.23	0.09		
19	18		0.92	36.66	1.54	0.93				56.84	0.9	0		1.51	0.29	0.21	0.02		
20	19		0.88	23.74	1.38	0.72				70.16	0.75	0		1.62	0.41	0.25	0.05		
21	20		5.14	21.81	2.11	0.88				66.88	0.61	0		1.38	0.32	0.26	0.51		
22	21		0.79	23.45	1.39	0.85				71.15	0.43	0		1.51	0.33	0.05	0.02		
23	22		5.22	43.14	3.06	2.19				42.31	1.18	0		1.2	0.57	0.69	0.3		
24	23		6.81	19.9	2.93	0.91				62.66	0.29	0		1.58	2.46	0.65	0.11		
25	24		0.7	21.7	1.52					73.61	0.76	0		1.22	0.4	0	0		
26	25		1.43	24.05	1.4					70.27	0.79	0		1.03	0.49	0.32	0.12		
27	26		11.37	17.54	1.43	0.74				60.75	0.55	0		3.57	3.71	0.24	0.03		
28	27		1.24	47.44	0.36	0.78				47.3	0.55	0		1.84	0.14	0.07	0.1		
29	28		0.61	47.37	0.23					48.24	0.62	0		1.95	0.22	0.13	0.14		
30	29		2.39	40.7	0.77	0.77				46.09	0.63	0		1.94	2.88	0.29	0.15		
31	30		1.89	49.34	0.77	0.93				42.97	0.54	0		2.82	0.23	0.3	0.1		
32	31		1.44	41.73	0.33					52.97	0.53	0		2.39	0.24	0.13	0.16		
33	32		1.28	43.83	0.36					51.13	0.67	0		2.36	0.17	0.02	0.05		
34	33		12.21	40.71	3.01	0.71				38.94	0.66	0		1.64	0.04	0.99	0.98		
35	34		2.9	20.68	1.65					71.53	0.6	0		1.41	0.83	0.25	0.12		
36	35		0.69	19.42	1.09					76.03	0.71	0		1.43	0.09	0.23	0.13		
37	36		1.06	23.9	1.3	0.63				70.16	0.54	0		1.55	0.57	0.14	0.1		
38	37		4.59	19.8	2	1.08				68.48	0.67	0		1.77	0.61	0.61	0.08		

Data output from WinMIgob software giving the Fe^{2+} and Fe^{3+} cation contributions used to calculate the average amount of TiO and ulvöspinel (Method #2).

P	Q	R	S	T	U	V	W	X
Fe3+	Fe2+	Ti	Total	Ti/Total=TiO	Ave TiO	SD Ti	Ulvo	Ave Ulvo
0.118817	1.664692	0.889408	2.672918	0.33274815	0.197624	0.019036	0.998244	0.592873
0.561763	1.459448	0.664788	2.685998	0.24750134			0.742504	
0.655545	1.430715	0.565208	2.651468	0.21316784			0.639504	
0.684459	1.429593	0.592077	2.70613	0.21879108			0.656373	
0.701368	1.413226	0.54646	2.661054	0.20535461			0.616064	
0.719525	1.418686	0.594953	2.733164	0.21767923			0.653038	
0.74521	1.395956	0.517595	2.658762	0.19467536			0.584026	
0.750676	1.393689	0.524682	2.669047	0.19658027			0.589741	
0.760358	1.389809	0.508175	2.658341	0.19116226			0.573487	
0.760567	1.388264	0.510536	2.659366	0.19197647			0.575929	
0.761045	1.465529	0.547537	2.774111	0.1973738			0.592121	
0.766193	1.386013	0.501967	2.654173	0.1891239			0.567372	
0.76971	1.402341	0.527707	2.699758	0.19546462			0.586394	
0.771127	1.378898	0.50073	2.650755	0.18890107			0.566703	
0.771644	1.397414	0.504466	2.673523	0.18868956			0.566069	

Results from hysteresis loops showing magnetic saturation, magnetic remanence, and coercivity values from the entirety of the flow reported in scientific notation as well.

Sample	Magnetic Saturation (Am^2/kg)	Scientific	Remanence (Am^2/kg)	Scientific	Coercivity (T)	Scientific
22QSC1	7.46E-05	0.00007	2.41E-05	0.00002	1.42E-02	0.01419
22QSC2B	1.03E-04	0.00010	2.83E-05	0.00003	1.26E-02	0.01264
22QSC2B.2	1.52E-04	0.00015	4.96E-05	0.00005	1.03E-02	0.01034
22QSCD	2.79E-04	0.00028	7.18E-05	0.00007	1.15E-02	0.01150
22QSCD.2	1.28E-04	0.00013	3.89E-05	0.00004	1.36E-02	0.01364
22QSC3	1.28E-04	0.00013	3.89E-05	0.00004	1.36E-05	0.00001
22QSC3B	1.48E-04	0.00015	4.21E-05	0.00004	8.52E-06	0.00001
19QSC4-4	1.44E-04	0.00014	4.62E-05	0.00005	1.83E-02	0.01827
19QSC5-7	8.28E-05	0.00008	2.94E-05	0.00003	1.07E-02	0.01069
19QSC6.1B	8.98E-05	0.00009	3.79E-05	0.00004	2.53E-02	0.02531
22QSC4A	1.79E-04	0.00018	4.87E-05	0.00005	1.41E-02	0.01414
22QSC4B	2.69E-04	0.00027	6.06E-05	0.00006	8.85E-03	0.00885
22QSC5C	1.47E-04	0.00015	4.12E-05	0.00004	8.73E-03	0.00873
22QSC5E	2.44E-04	0.00024	3.95E-05	0.00004	5.28E-03	0.00528